Assessing LLMs models' knowledge of automotive cyberthreats benchmarking autoISAC framework

Publisher copyright

(Article begins on next page)

23 December 2025

RESEARCH

Modeling, simulation, and validation of E-scooter braking dynamics using multibody methods

Angelo Domenico Vella[1] · Elisa Digo[1] · Alessandro Vigliani[1]

Abstract
Electric kick scooters have recently emerged in the urban scenario as a key solution to the mobility challenges of big city centers. While some studies have explored e-scooter dynamics, the complex interaction between the vehicle and its rider remains insufficiently understood. This study presents a numerical analysis of e-scooter braking maneuvers using a multibody modeling approach. A detailed in-plane multibody system is developed in Matlab/Simscape environment, including a high-fidelity model of a commercial electric kick scooter equipped with a front wheel motor and a rear braking disc system. To describe the human body response to the braking stimulus and its influence on vehicle dynamics, a semi-active anatomical dummy model is integrated. The multibody system is tuned and validated through a dedicated and comprehensive experimental campaign, specifically set-up to encompass three braking intensities and to measure key characteristics involving the dynamics of both vehicle and rider. The tuning process is based on an optimization algorithm designed to minimize the discrepancies between experimental and numerical signals. The developed multibody model provides a robust tool for analyzing the e-scooter dynamics in various driving scenarios, offering valuable insights to enhance safety and comfort.

Keywords Stand-up electric kick scooter · Urban sharing mobility · Light vehicles · Longitudinal vehicle dynamics · Experimental on-road testing · Rider-machine interaction

1 Introduction

Urban mobility significantly influences quality of life, encompassing environmental well-being and accessibility. In line with the growing interest in affordable, lightweight, and eco-friendly transportation solutions [1], electric micro-vehicles (e-MVs) have been emerged as a highly efficient alternative to gas-powered vehicles [2–4]. Even though e-MVs are topologically different from each other, they are characterized by some common characteristics such as the extreme compactness and the integration in the vehicle layout of an electric wheel motor for partial or full driving assistance. Considering limited spaces such as workplaces and urban apartments, the portability and the storage of e-MVs are simplified by their

✉ A.D. Vella
  angelo.vella@polito.it

1 Politecnico di Torino, Department of Mechanical and Aerospace Engineering (DIMEAS), Corso
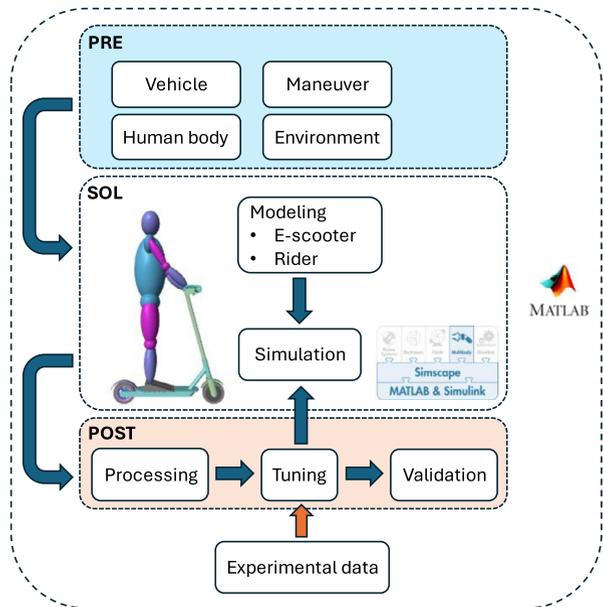   Duca degli Abruzzi 24, 10129, Turin, Italy

reduced size and foldability. Among e-MVs, electric kick scooters (e-scooters) are particularly popular, driven by their introduction as sharing services in metropolitan areas [5, 6]. Indeed, the integration of personal and shared e-scooters with public transport system is very useful to reduce the so called "last-mile gap" issue caused by urbanization [7]. However, features like stand-up riding posture and small tires distinguish e-scooters from other motorized two-wheelers, presenting unique challenges in safety and ride comfort [8].

The dynamic behavior of motorized two-wheeled vehicles, such as bicycles and motorcycles, has been extensively studied, often focusing on rider-vehicle interactions using multibody modeling techniques. For instance, the bicycle-rider system has been modeled through a multibody approach for studying the braking dynamics [9] and for identifying the rider's upper body motion [10]. Similarly, the motion of the motorcycle rider has been investigated developing virtual 3D models for examining the influence of the posture on discomfort, stiffness and pain [11, 12]. In contrast, specific studies on e-scooters have not yet been thoroughly conducted. Preliminary works have developed multibody models of an electric kick scooter including toroidal wheels and suspension systems [13] or more simple layouts for evaluating the performance when climbing small bumps [14]. Other studies have addressed vertical dynamics on lumped and distributed road irregularities [15, 16] and longitudinal dynamics [17] including a lumped parameter rider model. Riding comfort and stability are critical aspects of e-scooter mobility, with studies on the effects of road surface [18] and speed [19], and vibration comparison with other e-MVs like e-bikes [20]. Rider stability during common maneuvers has also been evaluated in controlled environments [21]. The ability of the e-scooter in filtering vibrations represents a recent topic of interest. Recent works have focused on vibrations transmitted by the e-scooter to the rider, employing methodologies for ride comfort and health assessment [22, 23]. Experimental studies have further explored the vibrational impact on riders [24–26], considering different users and driving conditions in realistic urban scenarios.

Overall, the research community has primarily approached e-scooter mobility from the perspective of vehicle, focusing on longitudinal and vertical dynamics, stability, and vibrations. However, the distinctive inertia distribution of the e-scooter/rider system, which is heavily shifted towards the rider, requires an in-depth analysis of human body motion. This investigation is crucial not only for achieving a comprehensive understanding of the coupled dynamics between the rider and the vehicle, but also for addressing critical factors that influence vehicle performance, maneuverability, and safety. A clearer insight into these aspects, which is essential to improve both control strategies and risk mitigation in dynamic riding scenarios, is still missing. In this research framework, multibody system approach represents a useful computational tool for simulating human body kinematics and dynamics, hence providing a strong foundation for vehicle design and optimization [27–29]. Moreover, wearable technologies such as magnetic-inertial measurement units (MIMUs) offer a cost-effective and non-invasive solution for capturing human motion during outdoor e-scooter riding, by collecting data from embedded triaxial accelerometers, gyroscopes, and magnetometers [30–32].

A preliminary study applying the multibody approach and MIMUs on the braking maneuvers has demonstrated the significant influence of the rider's motion on the dynamics of the e-scooter [33]. However, this work has two main limitations: (i) the analysis consists only of an emergency braking; (ii) the multibody rider model employed simplified control logic for the human body joints. To address these limitations, the present study extends the analysis of the e-scooter/rider system under braking conditions. A comprehensive in-plane model has been developed and validated using experimental data in Matlab/Simscape Multibody [34]. A healthy male subject has performed braking maneuvers of varying intensities (light,

Fig. 1 Simulation workflow

medium, heavy), with key dynamics and kinematics signals recorded for model tuning and validation through an optimization algorithm.

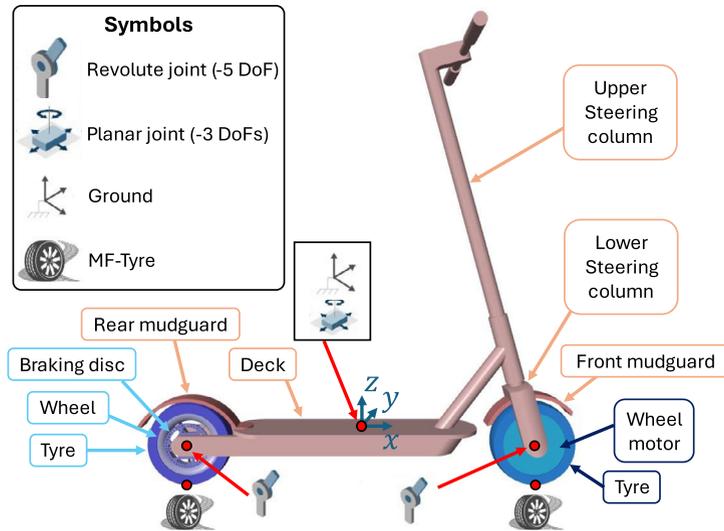The key novelties of this research include:

- the development of the model of a commercial e-scooter, incorporating experimentally identified driving and braking characteristics;
- the integration of an anatomical dummy system as rider with semi-active joint control;
- the tuning and the validation of the entire system based on the experimental data acquired in realistic driving scenarios;
- the implementation of an optimization-based tuning process to enhance model accuracy;
- the experimental validation using real-world data from braking scenarios.

The paper is structured as follows. First, the multibody model of the system composed of the e-scooter and the rider is presented. Then, the experimental campaign is described focusing on sensor set-up, test procedure, and data processing. Subsequently, the optimization-based tuning methodology is outlined. Finally, experimental-numerical comparisons are discussed, followed by conclusions.

2 Multibody modelling

The simulation workflow, specifically designed for this study, is illustrated in Fig. 1 and comprises three distinct phases implemented in Matlab R2024a: pre-processing (*PRE*), modeling and simulation (*SOL*), and post-processing (*POST*). The pre-processing phase involves defining key elements essential for the simulation:

- *vehicle:* includes the inertial properties of the components, the characteristics of the electric motor and the mechanical braking system;
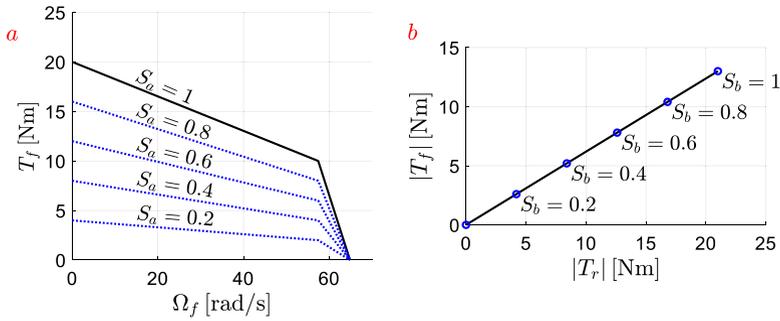
Fig. 2 E-scooter multibody model

- *human body:* encompasses the geometries of the human body segments, the initial conditions, and the equilibrium configurations of the body joints;
- *maneuver:* includes the driving inputs, i.e. the accelerator and the brake commands, and the initial condition for the vehicle velocity and wheels;
- *environment:* specifies the geometry of the road on which the vehicle performs the maneuver.

The virtual *modeling* and the time-domain *simulation* are conducted in Matlab/Simscape Multibody. The multibody system integrates the *e-scooter* and its *rider*, enabling dynamic interaction between them. The signals coming from both the vehicle and rider are collected during the simulation and analyzed in the post-processing phase: the numerical data monitored during the simulations are combined with the experimental data acquired during physical tests for the model *tuning* and *validation*. This comprehensive workflow ensures an accurate and reliable analysis by seamlessly integrating numerical simulations with real-world experimental data. For sake of compactness, the inertial properties of the vehicle components and the geometries of the human body segments are included in Appendix A and B respectively.

2.1 Electric kick scooter

The e-scooter multibody system, depicted in Fig. 2, consists of three main sub-systems, each comprising multiple rigid bodies. These components have been preliminary modelled in SolidWorks 2023 CAD environment and subsequently imported in Matlab/Simscape Multibody:

- the deck, the lower and upper parts of the steering column, and the front and rear mudguards;
- the wheel motor and the tire at the front;
- the wheel, the braking disc, and the tire at the rear.

Fig. 3 Torque characteristics included in the e-scooter model: driving characteristic of the motor (a) and braking characteristic due to the motor and the braking system (b)

The deck sub-system is connected to the front and rear wheel sub-systems via two kinematic revolute joints. Since the simulated maneuver does not involve any steering motion, the steering column is rigidly clamped to the deck. Additionally, to simplify the model, lateral (translation along y axis), lean (rotation around x axis), and yaw (rotation around z axis) motions of the vehicle are constrained using a kinematic planar joint between the deck and the ground. This configuration results in an in-plane two-wheeled vehicle system possessing five Degrees of Freedom (DoF), defined as follows:
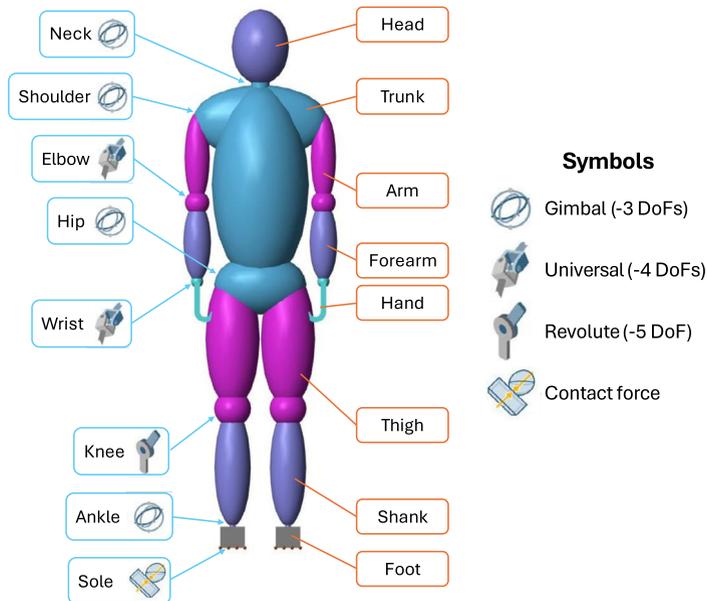
- longitudinal motion of the deck sub-system (translation along x axis);
- vertical motion of the deck sub-system (translation along z axis);
- pitch motion of the deck sub-system (rotation around y axis);
- spinning motion of the front wheel sub-system;
- spinning motion of the rear wheel sub-system.

To simulate tire-ground interactions, MF-Tyre 6.2 module is employed [35]. For sake of compactness, a detailed overview of the inertias of the vehicle components included in the model along with tyre longitudinal force versus the slip is provided in Appendix A. This detailed and constrained setup ensures that the model accurately captures the in-plane dynamics of the e-scooter during the braking maneuvers.

The electric motor and the braking system of the vehicle have been experimentally characterized and detailed in [17]. The torque characteristics integrated into the e-scooter model are illustrated in Fig. 3:

- Fig. 3a depicts the torque T_f applied by the electric motor to the front wheel under driving condition, as function of the acceleration command S_a and the angular velocity of the front wheel ω_f;
- Fig. 3b illustrates the module of the torques applied to the front wheel by the motor, $|T_f|$, and to the rear wheel by the mechanical braking system, $|T_r|$, under braking condition, as function of the braking command S_b.

In the real vehicle, S_a corresponds to the position of the accelerator roller and partialize the electric motor characteristic ($S_a = 1$, represented by black curve in Fig. 3a). Conversely, S_b represents the position of the braking lever. Although the braking mechanism at the front and at the rear may appear independent, the resulting braking torques, $|T_f|$ and $|T_r|$, are interconnected through a proportional relationship.
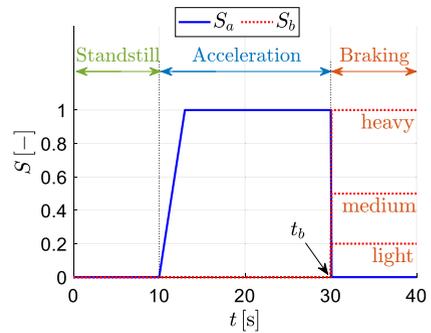
Fig. 4 Rider multibody model

2.2 Rider

As illustrated in Fig. 4, the rider is modelled as multibody system comprising 14 rigid bodies and 13 kinematic joints, listed by blue and red contoured boxes, respectively. The rider's upper body includes 9 rigid segments: *head*, *trunk*, right and left *arms*, right and left *forearms*, and right and left *hands*. The rider's lower body consists of 7 rigid segments: right and left *thighs*, right and left *shanks*, and right and left *feet*. The dimensions of the human body segments are based on those of the actual rider and are documented in Appendix B. A legend detailing the symbols used to represent different joint types is provided on the right side of Fig. 4. The following joints are incorporated into the human body model:

- *neck*, *shoulders*, *hips*, and *ankles* (gimbal joint): three translational DoFs are constrained, modeled as a gimbal joint;
- *elbows* and *wrists*: three translational and one rotational DoF are constrained, modeled as a universal joint;
- *knees*: a single rotational DoF is left free, modeled as a revolute joint.

The rider model, considered as standalone system, has a total of 37 degrees of freedom (DoFs). The interface between the vehicle and the human body is modeled at the hands and feet.

- Two kinematic revolute joints connect the hands of the rider to the steering handlebar of the e-scooter.
- 3D contact forces are integrated between the soles of the rider's shoes and the floor of the deck. This interaction is modeled using the penalty method, which generates a normal force that minimizes interpenetration between the contacting geometries and Coulomb frictional force that lies in the contact plane.

Fig. 5 Driving input in the braking maneuver simulation

Consequently, the total number of DoFs for the combined system is 32.

The torque applied to the j-th DoFs of the i-th rider's joint, T_{ij}, is expressed in Equation (1) and is composed of two contributions.

- S_{ij} ensures that the rider remains in the desired configuration under static conditions, i.e., under the action of gravitational forces only. This term depends on the current joint configuration vector $q(t)$, the reference configuration q_0, and the mass distribution of the human body model.
- D_{ij} governs the rider's response to dynamic effects, such as inertial forces generated during vehicle maneuvers. This term is modeled using proportional and derivative control and is defined by the gains p_{ij} and d_{ij}, as detailed in Equation (2).

Both S_{ij} and D_{ij} are time-varying and depend on the actual posture of the rider.

$$T_{ij}\left(q(t), q_0\right) = S_{ij}\left(q(t), q_0\right) + D_{ij}\left(q\left(t\right), \dot{q}(t), q_0\right) \tag{1}$$

$$D_{ij} = p_{ij}\left(q_{ij}(t) - q_{ij,0}\right) + d_{ij}\dot{q}_{ij}(t) \tag{2}$$

2.3 Braking simulation

Fig. 5 shows the accelerator, S_a, and the braking, S_b, inputs in the three phases of the braking simulation. The maneuver begins with the e-scooter in standstill condition, where both inputs are set to zero ($S_a = 0$, $S_b = 0$). During this phase, labeled *Standstill* in Fig. 5, the system is maintained in this state for 10 s to allow it to settle. Subsequently, the velocity is increased by gradually raising S_a to 1 over a period of 5 s. This phase, denoted *Acceleration* in Fig. 5, is sustained for 15 s to ensure the vehicle reaches its maximum velocity of 25 km/h and allows the rider to achieve a steady equilibrium. At $t = t_b$, S_a is abruptly set to 0 and at the same time S_b is adjusted to simulate different braking intensities. The braking levels correspond to three scenarios: heavy ($S_b = 1$), medium ($S_b = 0.5$) and light ($S_b = 0.2$). This phase (referred as Braking in Fig. 5) ends in 10 s.
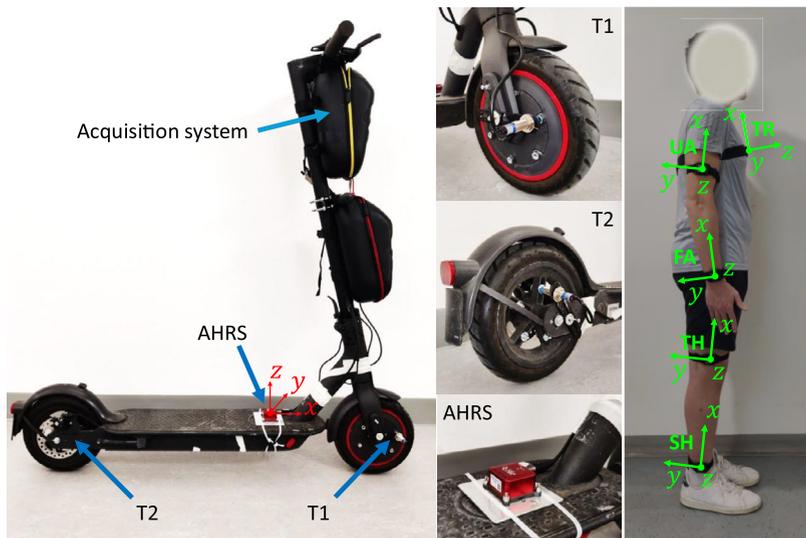
A variable-step integrator, ode23t, designed for moderately stiff differential-algebraic equation (DAE) problems is utilized to solve the system dynamics [36]. The integrator settings, determined through a convergence analysis and detailed in Table 1, are adopted to ensure accurate results and reduced simulation time ($\sim$60 s).

3 Model tuning

The model tuning involves the identification of the unknown parameters of the human body model, i.e. the joint parameters p_{ij} and d_{ij}, during the braking maneuver. To achieve this,

Table 1 Integrator settings

Maximum step size [s]	10^{-2}
Minimum step size [s]	10^{-8}
Initial step size [s]	10^{-6}
Relative tolerance	10^{-5}
Absolute tolerance	10^{-5}

Fig. 6 Sensor setup

an experimental campaign is conducted to collect data from the e-scooter and the rider in the three different braking scenarios (heavy, medium, light). An optimization process is then designed to minimize the mismatch between numerical simulations and experimental signals, ensuring accurate parameter estimation.

3.1 Experimental tests and data processing

The on-road tests are conducted by a young healthy male (27 years old, 76 kg, BMI = 23.5 kg/m^2) riding a commercial e-scooter, Xiaomi Pro II. The measurement setup used during the tests is shown in Fig. 6. Two inductive tachometers are employed to measure the angular velocity of the wheels (Ω), T1 at the front and T2 at the rear. An SBG Ellipse-A Attitude Heading Reference System (AHRS) is positioned on the deck of the e-scooter to monitor the vehicle longitudinal acceleration (a_x). All vehicle signals are synchronously acquired by Siemens SCADAS XS data acquisition system, fixed on the steering column of the e-scooter, with a sampling frequency of 200 Hz. For human motion analysis an inertial system (OpalTM APDM, USA) comprising five wireless magneto-inertial measurement units (MIMUs) is used. Based on the findings reported in [24, 25], which demonstrated that the parallel-feet posture statistically minimizes vibration transmissibility to the rider's upper body, this configuration has been adopted for the experimental campaign. While acknowledging that other postures (e.g., staggered stance) are commonly observed in daily use, the

parallel-feet stance was selected to ensure consistency and reduce complexity, given the specific scope of the study focused on in-plane braking dynamics. Therefore, the MIMUs are fastened with APDM bands on the trunk (TR) and the right side of the rider body in correspondence of the upper arm (UA), the forearm (FA), the thigh (TH), and the shank (SH). The MIMU reference frames (highlighted in green in the right panel of Fig. 6) correspond to the neutral position of the rider. Each unit is oriented such that its local x axis is aligned with the longitudinal axis of the corresponding human body segment:

- from the pelvis to the neck for TR;
- from the center of the elbow to the center of the shoulder for UA;
- from the center of the wrist to the center of the elbow for FA;
- from the center of the knee to the center of the hip for TH;
- from the center of the ankle to the center of the knee for SH.

The angular motion around the x axis represents the intra-extra rotation of each segment around its longitudinal axis. Considering the trunk, the thighs, and the shanks, the angular motion around the y and z axes represent the flexion-extension and the abduction-adduction of each segment around their medio-lateral and anterior-posterior axes, respectively. When riding the e-scooter, the human body transitions from the neutral position to the typical riding position, moving the upper arms and forearms to grip the handlebars. In this configuration, the angular motion around the y and the z axes represent the abduction-adduction and the flexion-extension of both upper arm and forearm around their anterior-posterior and medio-lateral axes, respectively. Each Opal^{TM} APDM MIMU is used to monitor the components of the angular velocities ω of the five human body segments (range of ± 2000 °/s). Signals are acquired at a sampling frequency of 200 Hz via Motion Studio^{TM} (APDM, USA) using Bluetooth communication between MIMUs and the host machine. The synchronization between Opal and SCADAS acquisition systems is obtained through an analogue trigger signal at the beginning of each test.

The experimental tests mirrored the numerical simulations as illustrated in Fig. 5 and consist of three phases, i.e. acceleration from standstill condition and braking after the velocity settling. The maneuver is performed at three different levels (light, medium, and heavy) based on the experience of the rider. Each braking level is tested 3 times to verify repeatability.

To reduce the experimental signal noise, a digital filter with a cut-off frequency of 20 Hz, is applied to the human body signals in post-processing. A qualitative analysis of the experimental results reveals significant trends in the angular motion of the trunk around y axis and the thigh and the shank around the z axis. These signals are subsequently used for both model optimization and validation.

Toward the end of braking, the experimental signals exhibit small oscillations caused by vehicle lateral instability as the system slows to a stop. In addition, further disturbances occur when the rider adjusts his posture after stopping, which cannot be replicated by the current multibody model. Since the study focuses on the active braking phase, the authors propose truncating the data to exclude this final, less relevant portion of the time histories.

3.2 Model optimization

The tuning of the multibody model aims to align the dynamics of e-scooter/rider multibody system with the experimental outcomes. To achieve this, the model is integrated into an optimization process designed to minimize the mismatch between experimental and numerical

results. The optimization problem is formulated in Equation (3),

$$\mathbf{x}_o = \arg\min C(\mathbf{x}) : \underline{\mathbf{x}} \leq \mathbf{x} \leq \overline{\mathbf{x}} \subseteq R^n \tag{3}$$

where:

- $\mathbf{x}$ are the optimization variables;
- $C(\mathbf{x})$ is the cost function;
- $\mathbf{x}_o$ is the optimal set that minimize $C(\mathbf{x})$;
- $\underline{\mathbf{x}}$ and $\overline{\mathbf{x}}$ are the lower and upper bounds of $\mathbf{x}$.

The optimization variables $\mathbf{x}$ include the proportional (p_{ij}) and derivative (d_{ij}) gain coefficients which control the in-plane rider motion:

- the flexion/extension of the ankle;
- the flexion/extension of the knee;
- the flexion/extension of the hip;
- the flexion/extension of the shoulder;
- the abduction/adduction of the shoulder;
- the intra/extra rotation of the shoulder.

The constrained nonlinear multivariable cost function $C(\mathbf{x})$ is shown in Equation (4),

$$C(\mathbf{x}) = \sum_{k=1}^{N} \varepsilon_k(\mathbf{x}) \tag{4}$$

where ε_k quantifies the error between specific numerical $(s_{k,n})$ and experimental $(s_{k,e})$ signals, including:

- the vehicle longitudinal acceleration (a_x);
- the medio-lateral angular velocity of the trunk (ω_y);
- the medio-lateral angular velocity of the thigh (ω_z);
- the medio-lateral angular velocity of the shank (ω_z).

The error ε_k is evaluated as the sum of the normalized difference between the experimental and numerical maxima (u), minima (v), and their time gap, as shown in Equation (5):

$$\varepsilon_k = \varepsilon_{k,u} + \varepsilon_{k,v} + \varepsilon_{k,\tau} = \left| \frac{u_{k,n} - u_{k,e}}{m_{k,e}} \right| + \left| \frac{v_{k,n} - v_{k,e}}{m_{k,e}} \right| + \left| \frac{\tau_{k,n} - \tau_{k,e}}{|\tau_{k,e}|} \right| \tag{5}$$

$\varepsilon_{k,u}$, $\varepsilon_{k,v}$ and $\varepsilon_{k,\tau}$ are saturated to 1 to ensure the same weight to three different error contributions. The terms u_k, v_k, m_k and τ_k are computed in Equations (6) to (9)

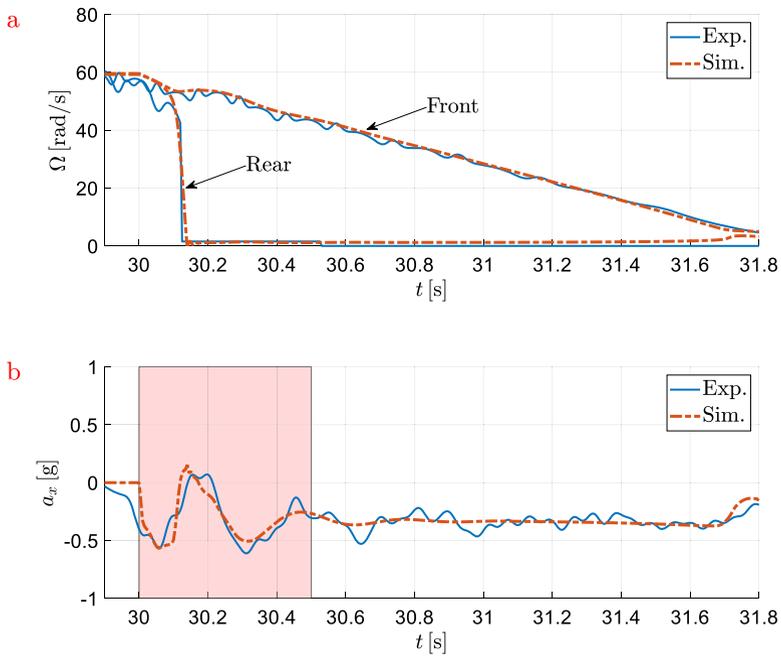$$u_k = \max(s_k) \qquad\qquad t \in [t_b, t_b + T_0] \tag{6}$$

$$v_k = \min(s_k) \qquad\qquad t \in [t_b, t_b + T_0] \tag{7}$$

$$m_k = \max(|s_k|) \qquad\qquad t \in [t_b, t_b + T_0] \tag{8}$$

$$\tau_k = \tau(s_k = u_k) - \tau(s_k = v_k) \tag{9}$$

The error ε_k is evaluated during the first $T_0 = 0.5$ s of the heavy braking test, starting from the beginning of the braking phase at $t = t_b$. The multivariable optimization problem described in Equation (3) is solved by combining a probabilistic search method (Genetic Algorithm, GA) with a direct search method (Pattern Search, PS): this strategy enables exploring
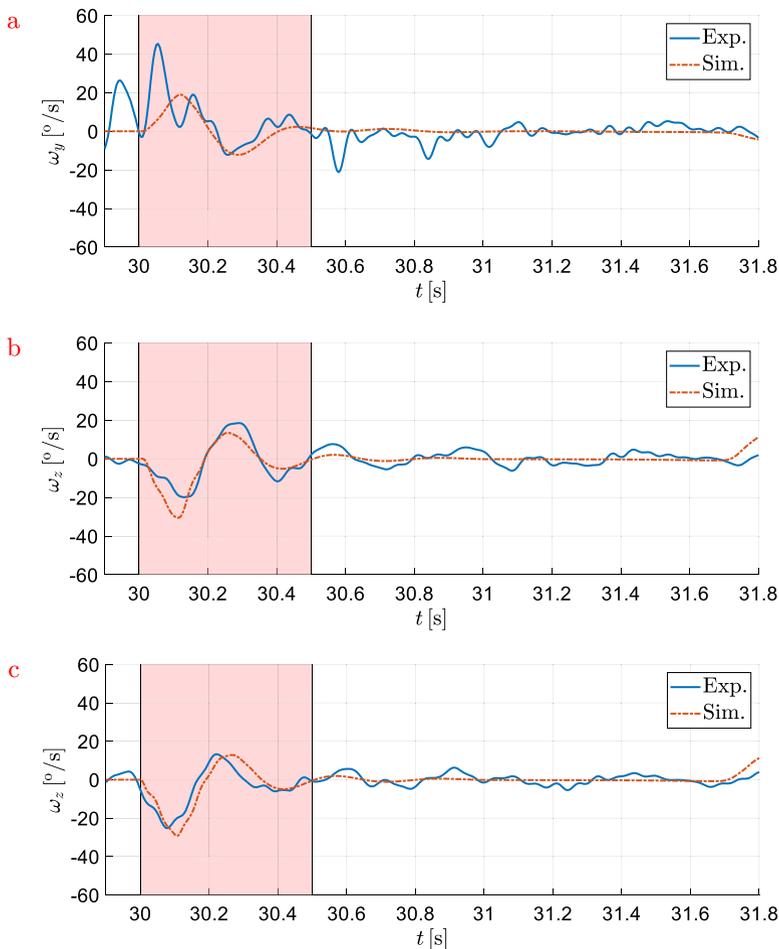
Fig. 7 Experimental and simulated signal comparison: wheel angular velocities (a) and longitudinal acceleration (b) in the heavy braking maneuver

the solution space, reduces the risk of converging to local minima, and improves computational efficiency. Specifically, the optimization process begins with GA, which starts from a randomly generated initial population of variable sets. Upon reaching one of its termination criteria, the best solution from GA is used as the initial guess for the PS algorithm. The final output of the PS phase defines the optimal variable set $\mathbf{x}_o$. The lower bounds $\underline{\mathbf{x}}$ are defined to ensure that p_{ij} and d_{ij} gains remain strictly positive. The upper bounds $\overline{\mathbf{x}}$ are set to guarantee sufficient mobility in the human body joints. After the optimization process, the optimal solution $\mathbf{x}_o$ is verified to lie well within the feasible range, remaining significantly below the upper limits. For sake of brevity, further details on the optimization settings are provided in Appendix C. To verify convergence toward a global minimum, the optimization routine is executed multiple times with different randomized initial populations, and the consistency of the resulting $\mathbf{x}_o$ values is assessed.
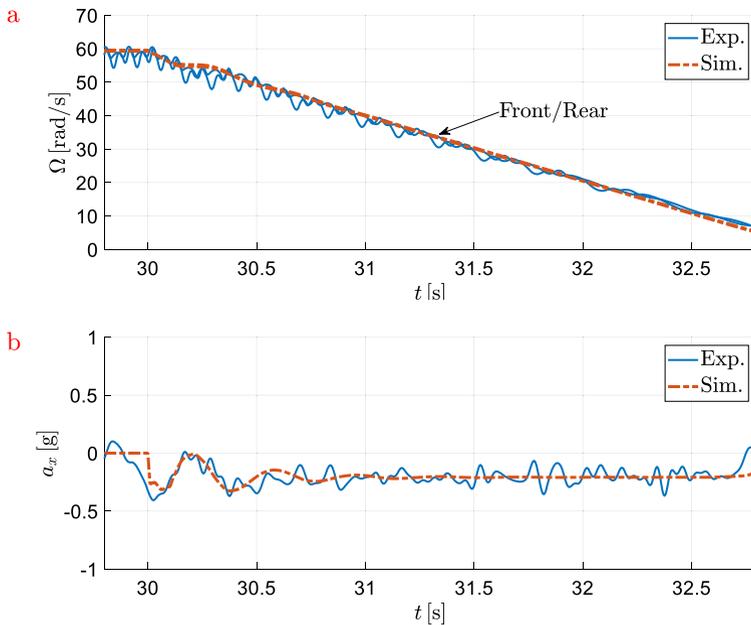
4 Results and discussion

Fig. 7 and Fig. 8 represent the experimental-numerical comparison in terms of vehicle and human body signals during the heavy braking maneuver: the experimental signals are shown in solid blue line while the numerical data are shown in dashed orange line. A red shaded area is included to highlight the time interval used for the model tuning. In general, the numerical signals are in good agreement with the experimental results apart from some residual experimental noise. Fig. 7a shows the angular velocity of the wheels while Fig. 7b illustrates the longitudinal acceleration of the deck. As depicted by Fig. 7a, the rear wheel

Fig. 8 Experimental and simulated signal comparison: trunk angular velocities around y local axis (a), thigh angular velocity around z local axis (b) and shank angular velocity around z local axis in the heavy braking maneuver (c)

encounters the full-locking condition during the maneuver due to the applied braking torque, and this occurs both in the experimental test and in the simulation. On the other hand, the front wheel does not reach the locking condition. The longitudinal acceleration, shown in Fig. 7b, is characterized by oscillations which are a consequence of the rider motion as demonstrated in [17, 33].
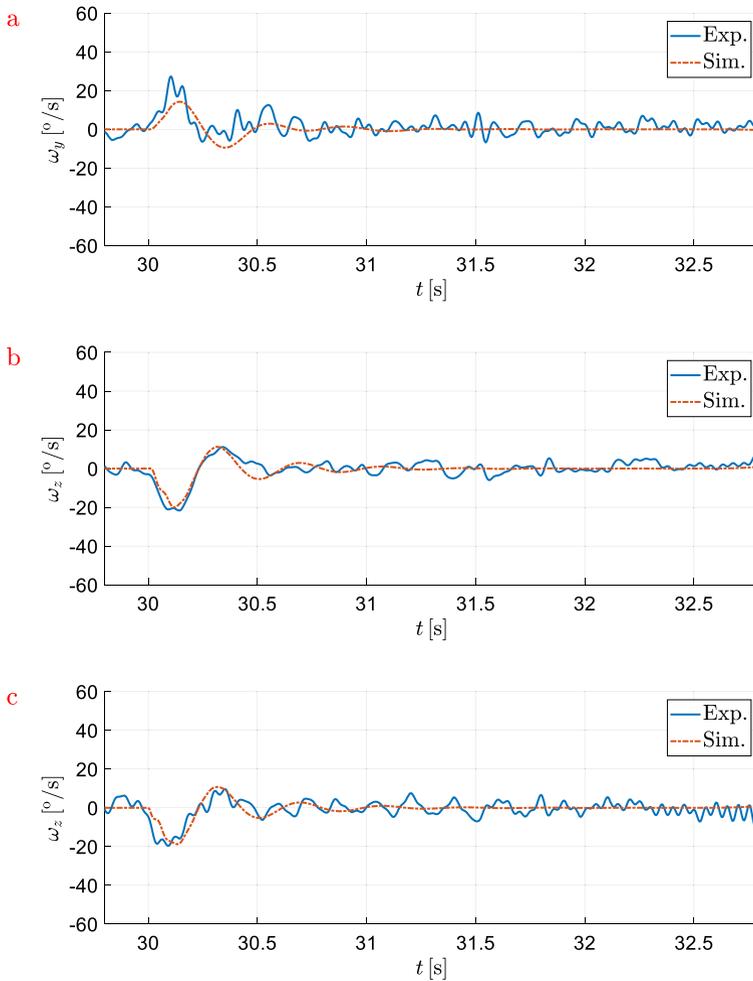
Fig. 8 represents the angular velocities around the medio-lateral axis of the trunk (Fig. 8a), the thigh (Fig. 8b) and the shank (Fig. 8c). A good correlation between the experimental and the numerical signals during the heavy braking maneuver can be observed also for the human body angular velocities. Considering the angular velocity of the trunk, a positive peak (0.8 rad/s for the experimental signal and 0.33 rad/s for the numerical signal) corresponds to a backward rotation as response to the vehicle deceleration. This reaction is then balanced by a forward rotation (negative peak of approximately -0.2 rad/s for both the experimental and the numerical signals) to maintain the equilibrium until the end of the

Fig. 9 Experimental and simulated signal comparison: wheel angular velocities (a) and longitudinal acceleration (b) in the medium braking maneuver

maneuver. Considering the angular velocities of both thigh and shank, the forth-back oscillation of the trunk is also visible in the legs with a negative peak corresponding to the extension of the hip and the flexion of the ankle (thigh: -0.35 rad/s for the experimental signal and -0.53 rad/s for the numerical signal; shank: -0.44 rad/s for the experimental signal and -0.50 rad/s for the numerical signal), and a positive peak corresponding to the flexion of the hip and the extension of the ankle (thigh: 0.32 rad/s for the experimental signal and 0.23 rad/s for the numerical signal; shank: 0.23 rad/s for both the experimental and the numerical signals). This evidence suggests that the rider's pelvis tends to get closer to the e-scooter handlebar in the first phase of the braking; in a second phase the rider tends to achieve a new equilibrium configuration.
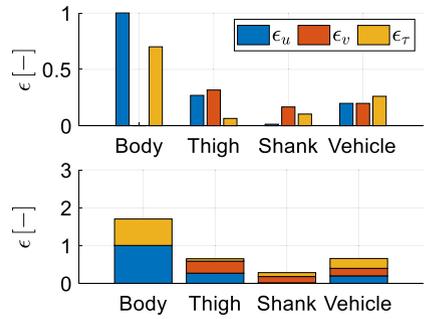
Similarly to the heavy braking maneuver, experimental and numerical data from both the vehicle and the human body are compared also for the medium and the light braking maneuvers. For sake of brevity, the experimental-numerical comparison related to the light braking maneuver is reported in Appendix D (Fig. 16 and Fig. 17). Fig. 9 shows the wheel angular velocities (Fig. 9a) and the longitudinal acceleration of the e-scooter (Fig. 9b) during the medium braking maneuvers. In this braking condition, the rear wheel does not lock, and its angular velocity is similar to the front wheel angular velocity. In addition, the angular velocities around the medio-lateral axis of human segments (trunk, thigh and shank) are reported in Fig. 10. The same good correlation existing between the experimental and the numerical human body signals can be observed also for the medium and the light braking maneuvers. The trunk angular velocity presents an unbalancing backward response with a positive peak (medium: 0.47 rad/s for the experimental signal and 0.22 rad/s for the numerical signal; light: 0.24 rad/s for the experimental signal and 0.14 rad/s for the numerical signal) smaller than the peak of the heavy braking maneuver. The following forward rotation of the trunk

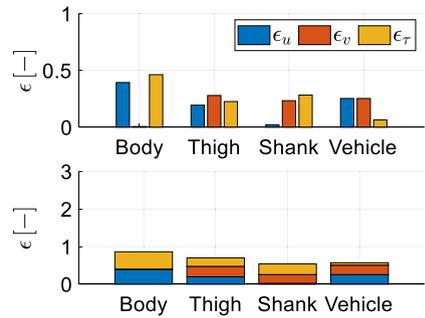**Fig. 10** Experimental and simulated signal comparison: trunk angular velocities around y local axis (a), thigh angular velocity around z local axis (b) and shank angular velocity around z local axis (c) in the medium braking maneuver

to maintain the equilibrium is expressed by a negative peak, which is smaller with respect to the heavy braking maneuver (medium: -0.11 rad/s for both the experimental and the numerical signals; light: -0.07 rad/s for both the experimental and the numerical signals). Similarly to the trunk, also the angular velocities of the thigh presents the same trend of the heavy braking maneuver with a first negative peak corresponding to the extension of the hip combined with the flexion of the ankle (medium: -0.36 rad/s for the experimental signal and -0.27 rad/s for the numerical signal; light: -0.27 rad/s for the experimental signal and -0.15 rad/s for the numerical signal) followed by a second positive peak corresponding to the flexion of the hip and the extension of the ankle (medium: 0.19 rad/s for the experimental signal and 0.12 rad/s for the numerical signal; light: 0.14 rad/s for the experimental signal and 0.05 rad/s for the numerical signal). The same trend is also visible for the angular velocities of the shank, with a negative peak (medium: -0.34 rad/s for the experimental signal
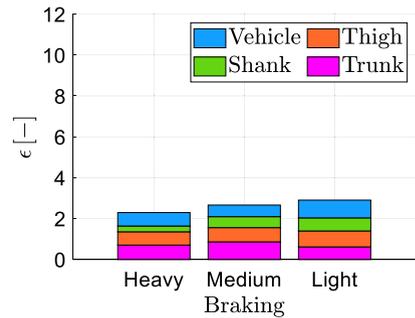
Fig. 11 Experimental-numerical error in the heavy braking maneuver

Fig. 12 Experimental-numerical error in the medium braking maneuver

Fig. 13 Experimental-numerical errors in the light, medium and heavy braking maneuvers

and -0.26 rad/s for the numerical signal; light: -0.24 rad/s for the experimental signal and -0.14 rad/s for the numerical signal) and a positive peak (medium: 0.15 rad/s for the experimental signal and 0.12 rad/s for the numerical signal; light: 0.08 rad/s for the experimental signal and 0.04 rad/s for the numerical signal). These values indicate that the rider behaves in the same way during the braking maneuver on the sagittal plane independently of the intensity of the braking itself. The difference is limited to the absolute value of the oscillations, which tends to decrease shifting from heavy to light maneuvers.

Fig. 11 to Fig. 13 depicts the errors expressing the difference between the numerical and experimental signals of the human (trunk, thigh, and shank $\omega_{y/z}$) and the vehicle (a_x) considering the maximum (ε_u), the minimum (ε_v), and their time distance (ε_τ) as shown in Equation (5). In detail, Fig. 11 and Fig. 12 present these errors for heavy and medium braking intensities, respectively. For sake of compactness, the errors related to the light braking are reported in Fig. 18 in Appendix D. Each figure consists of two panels: the top

Table 2 Coefficient of Pearson correlation for deck acceleration and rider's angular velocities

Body	Signal	Braking		
		Heavy	Medium	Light
Deck	a_x	0.8	0.5	0.2
Trunk	ω_y	0.5	0.7	0.9
Thigh	ω_z	0.9	0.9	0.5
Shank	ω_z	0.9	0.8	0.6

one compares the three error contributions across districts, while the bottom one illustrates their cumulative sums, emphasizing the contribution of each district to the overall error. In the first panels of the figures, apart from ε_τ of the body in the heavy braking maneuver and ε_τ of the vehicle in the light braking maneuver, all the other errors are lower than 0.5. Considering the sum of errors in the second panels, their values are at most equal to 0.86 apart from the trunk, which is lower than the maximum possible error equal to 3. The trunk total error increases from the heavy (1.7) to the medium (0.86) and light (0.61) braking. The thigh and the shank total errors increase from the heavy (0.65 for the thigh and 0.28 for the shank) to the medium (0.70 for the thigh and 0.54 for the shank) and to the light (0.80 for the thigh and 0.64 for the shank). Vehicle errors follow the opposite trend, decreasing from the heavy (0.66) to the medium (0.57) and to the light (0.56) braking maneuvers.

In Fig. 13 the total error for each braking intensity is presented highlighting the different contributions of human and vehicle signals. The total error slightly increases from the heavy (2.29) to the medium (2.66) and to the light (2.90) braking maneuvers, demonstrating that the proposed model behaves in the same way independently from the braking intensity. The cumulative error ranges from 2.6 to 3.3 and is significantly lower than its maximum possible value (12).

Table 2 contains the coefficients of Pearson correlation (R) calculated comparing the experimental and simulated signals in time domain (ω_y for human trunk, ω_z for the thigh and shank, a_x for the e-scooter deck) in the first 1 s of braking. These coefficients measure the strength and the direction of the linear relationship between two variables, identifying a moderate correlation with $0.5 \leq R \leq 0.7$, a strong correlation with $0.7 \leq R \leq 0.9$ and a very strong correlation with $R \geq 0.9$ [37, 38]. Considering human segments, all correlation coefficients are at least equal to 0.5 with an average value of 0.75 (standard deviation of 0.17), demonstrating from moderate to excellent performance of the model depending on the intensity of the braking maneuver. In detail, the correlation is influenced in a different way based on the considered human body segment. Indeed, the correlation for the trunk angular velocity increases while passing from heavy ($R = 0.5$) to light ($R = 0.9$) intensity. On the contrary, the correlations of the leg angular velocities decrease with the reduction of the braking intensity from heavy ($R = 0.9$ for the thigh and $R = 0.9$ for the shank) to medium ($R = 0.9$ for the thigh and $R = 0.8$ for the shank) and to light ($R = 0.5$ for the thigh and $R = 0.6$ for the shank). Results suggest that the model performs better for the trunk during a light braking maneuver and for the legs during a heavy braking maneuver. Considering the acceleration of the e-scooter deck, the correlation has an average value of 0.5 (standard deviation of 0.3). It decreases with the reduction of the braking maneuver intensity from heavy ($R = 0.8$) to light ($R = 0.2$). The observed trend can be attributed to the worsening signal-to-noise ratio associated with lower braking maneuver intensity. Consequently, despite the underlying similarity in the curve trends, noise-induced fluctuations significantly reduce the resulting correlation.
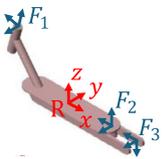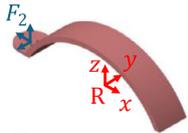
5 Conclusions

In this paper, a comprehensive simulation workflow including a multibody system of the e-scooter/rider system is presented. The model, developed in Matlab environment, is specifically designed to replicate the in-plane dynamic behavior of both the vehicle and the human body in braking maneuvers of different intensities. A key aspect of the study is the model tuning and validation, which are achieved through a dedicated experimental campaign collecting data from both the e-scooter and the rider's body during braking maneuvers. In detail, braking maneuvers of three different levels conducted by a healthy young male rider are exploited to record inertial signals, i.e. angular velocities and linear accelerations, characterizing both the e-scooter longitudinal dynamics and the human body motion. An optimization process is successfully developed to fine-tune the dynamic response of the human body joints affecting the in-plane motion of the rider system. This algorithm aims at minimizing the discrepancy between experimental and numerical data, providing a realistic representation of the interaction between the rider and the vehicle in braking scenarios. The final model is able to simulate braking maneuvers of different intensities, highlighting good replicability with respect to experimental evidence. Overall, the proposed study offers a practical and robust tool for analyzing the coupled dynamics of the e-scooter and its rider in one of the most common riding posture, paving the way for future advancements for safety improvements and comfort optimization. Current efforts are focused on integrating a tire-ground contact formulation suitable for ride comfort analysis and extending the multibody system to support full 3D simulations.
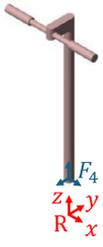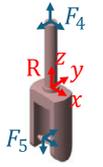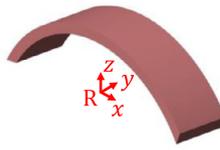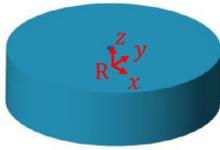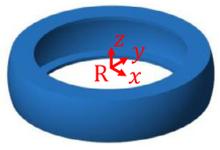
Appendix A: e-scooter data

In this Appendix the data related to the e-scooter model are collected. Table 3 shows the inertial properties of the mechanical components of the e-scooter. The location of the center of mass (G) of each component is expressed in function of the main reference frame (R)

Table 3 Inertial data of the component of the e-scooter

Component	Picture	G location [m]	Mass [kg]	$I_{G,ij}$ [kg m$^2 \cdot 10^{-3}$]
Deck		$x_G = 0.016$ $y_G = 0$ $z_G = -0.004$	6.970	$I_{G,xx} = 29.9$ $I_{G,yy} = 302.6$ $I_{G,zz} = 288.8$ $I_{G,xy} = 0$ $I_{G,xz} = 38.5$ $I_{G,yz} = 0$
Rear mudguard		$x_G = -0.008$ $y_G = 0$ $z_G = 0.001$	0.180	$I_{G,xx} = 0.1$ $I_{G,yy} = 1.3$ $I_{G,zz} = 1.3$ $I_{G,xy} = 0$ $I_{G,xz} = 0$ $I_{G,yz} = 0$

Table 3 (*Continued*)

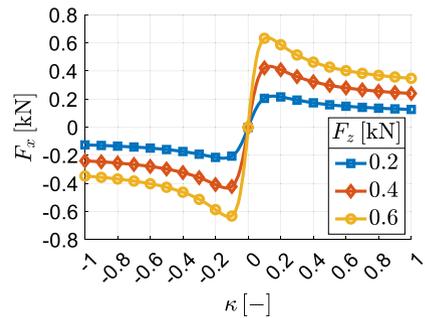| Component	Picture	G location [m]	Mass [kg]	$I_{G,ij}$ [kg m² · 10⁻³]
Upper steering column		$x_G = 0$ $y_G = -0.032$ $z_G = 0.687$	1.550	$I_{G,xx} = 82.8$ $I_{G,yy} = 88$ $I_{G,zz} = 10.6$ $I_{G,xy} = 0$ $I_{G,xz} = 0$ $I_{G,yz} = 9.4$
Lower steering column		$x_G = 0$ $y_G = 0$ $z_G = -0.03$	0.932	$I_{G,xx} = 6.8$ $I_{G,yy} = 7.4$ $I_{G,zz} = 1.1$ $I_{G,xy} = 0$ $I_{G,xz} = 0$ $I_{G,yz} = 0$
Front mudguard		$x_G = 0$ $y_G = 0.103$ $z_G = 0.015$	0.05	$I_{G,xx} = 0.3$ $I_{G,yy} = 0.2$ $I_{G,zz} = 0.2$ $I_{G,xy} = 0$ $I_{G,xz} = 0$ $I_{G,yz} = 0$
Motor		$x_G = 0$ $y_G = 0$ $z_G = 0$	3.085	$I_{G,xx} = 5.5$ $I_{G,yy} = 5.5$ $I_{G,zz} = 9.9$ $I_{G,xy} = 0$ $I_{G,xz} = 0$ $I_{G,yz} = 0$
Tire		$x_G = 0$ $y_G = 0$ $z_G = 0$	0.482	$I_{G,xx} = 2.5$ $I_{G,yy} = 2.5$ $I_{G,zz} = 4.8$ $I_{G,xy} = 0$ $I_{G,xz} = 0$ $I_{G,yz} = 0$

in red. The auxiliar reference frame (F) based on geometric features of the CAD parts are used for including the kinematic constraints. The moments of the inertial tensor, $I_{G,ij}$, are expressed in function of a reference system centered in G with the axes oriented such R.

Fig. 14 represents the steady-state tyre longitudinal force, F_x, versus the longitudinal slip κ for different vertical loads ($F_z = 0.2, 0.4, 0.6$ kN), implemented in the multibody model through MF-Tyre 6.2. The longitudinal slip of the tyre is evaluated according to

Table 3 (*Continued*)

Component	Picture	G location [m]	Mass [kg]	$I_{G,ij}$ [kg m$^2 \cdot 10^{-3}$]
Rear wheel		$x_G = 0$ $y_G = 0$ $z_G = 0$	0.551	$I_{G,xx} = 0.9$ $I_{G,yy} = 0.9$ $I_{G,zz} = 1.5$ $I_{G,xy} = 0$ $I_{G,xz} = 0$ $I_{G,yz} = 0$
Braking disc		$x_G = 0$ $y_G = 0$ $z_G = 0$	0.225	$I_{G,xx} = 0.2$ $I_{G,yy} = 0.2$ $I_{G,zz} = 0.4$ $I_{G,xy} = 0$ $I_{G,xz} = 0$ $I_{G,yz} = 0$

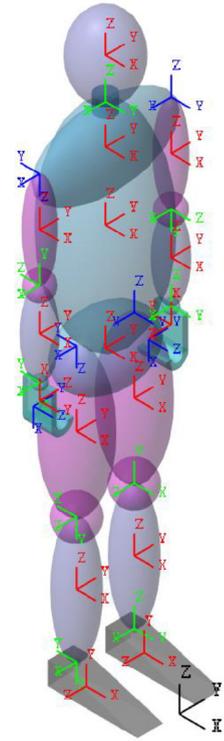**Fig. 14** Tyre longitudinal force in function of longitudinal slip for different vertical loads

Equation (10) where Ω is the angular speed, V_x is the longitudinal component of the velocity and r_e is the effective rolling radius [39].

$$\begin{cases} \kappa = 1 - \dfrac{V_x}{\Omega r_e} & \Omega r_e \geq V_x \\ \kappa = \dfrac{\Omega r_e}{V_x} - 1 & \Omega r_e < V_x \end{cases} \tag{10}$$

Appendix B: Rider data

Fig. 15 shows the rider's multibody model in its reference configuration (angles of the kinematic joints set to 0°). Red frames indicate the center of mass of the main human body segments; green frames highlight the location of the center of mass of human body joints and, when coincident, the corresponding kinematic joints; blue frames mark the position of the other kinematic joints. Except for the hands, feet and neck, all rigid bodies used to model the rider's body are characterized by ellipsoidal shapes. The dimensions, as well as the location of the bodies and kinematic joints according to a global reference system (black frame) are listed in Table 4.

Fig. 15 Rider model: reference frames of the body and kinematic joints

Table 4 Radii of the ellipsoidal bodies of the rider

Body	Dimensions [m]			Location		
				x [m]	y [m]	z [m]
Left/right Foot	0.28	0.23	0.07	−0.2	±0.1	0.02
Left/right ankle	0.01	0.01	0.01	−0.23	±0.1	0.07
Left/right lower leg	0.059	0.059	0.195	−0.23	±0.1	0.265
Left/right knee	0.06	0.06	0.06	−0.23	±0.1	0.46
Left/right upper leg	0.088	0.088	0.23	−0.23	±0.1	0.69
Left/right hip		−		−0.23	±0.1	0.92
Head	0.093	0.093	0.125	−0.23	0.0	1.655
Neck	0.03	0.05		−0.23	0.0	1.53
Core	0.158	0.158	0.33	−0.23	0.0	1.2
Chest	0.065	0.170	0.36	−0.23	0.0	1.41
Pelvis	0.1	0.15	0.33	−0.23	0.0	0.87
Left/right shoulder		−		−0.23	±0.215	1.44
Left/right arm	0.041	0.041	0.150	−0.23	±0.215	1.29
Left/right elbow	0.04	0.04	0.04	−0.23	±0.215	1.14
Left/right forearm	0.045	0.045	0.130	−0.23	±0.215	1.01
Left/right wrist	0.02	0.02	0.02	−0.23	±0.215	0.88
Left/right hand	0.1	0.09	0.018	−0.23	±0.215	0.83
Left/right grip		−		−0.23	±0.190	0.77

Table 5 Initial and equilibrium conditions of the kinematic joints of the rider model in the braking simulation

Joints	Initial/equilibrium conditions [∘]		
	$q_{x,0}$	$q_{y,0}$	$q_{z,0}$
Ankle	0.6	0.0	0.0
Knee	−1.0		
Hip	1.0	0.0	0.0
Neck	0.0	0.0	0.0
Shoulder	31.8	0.0	−29.6
Elbow	18.2	61.3	
Wrist	−7.9	40.9	
Grip	16.7		

Table 6 Tuned proportional and derivative gain coefficients of the human body joint

Joint	Motion	Coefficient	
		p [N m/rad]	d [N ms/rad]
Ankle	Flexion-extension	2.161	0.028
Knee	Flexion-extension	19.278	0.006
Hip	Flexion-extension	1.088	0.031
Shoulder	Flexion-extension	1.633	0.013
Shoulder	Abduction-adduction	21.274	0.180
Shoulder	Intra-extra rotation	2.930	0.193

Table 5 shows the initial and equilibrium conditions of the angles for each kinematic joint of the rider model integrated with the e-scooter.

All the bodies are modelled as homogeneous and characterized by a unique value of density (930 kg/m^3), tuned to replicate the mass of the real rider.

Table 6 shows the tuned proportional and derivative gain coefficient used for controlling the human body kinematic joint during the simulation

Appendix C: Optimization algorithms

Table 7 and Table 8 illustrate the parameters used in the Genetic Algorithm (GA) and Pattern Search (PS) optimization loop [40–43]. These settings are selected as trade-off between computational cost and convergence reliability.

Appendix D: Other results

Fig. 16 and Fig. 17 show the experimental-numerical comparison in the light braking maneuver. Fig. 16a depicts the angular velocity of the front and rear wheel while Fig. 16b illustrates the longitudinal acceleration of the deck.

Fig. 17a, Fig. 17b and Fig. 17c show the angular velocity around the medio-lateral axis of the trunk, thigh and shank.
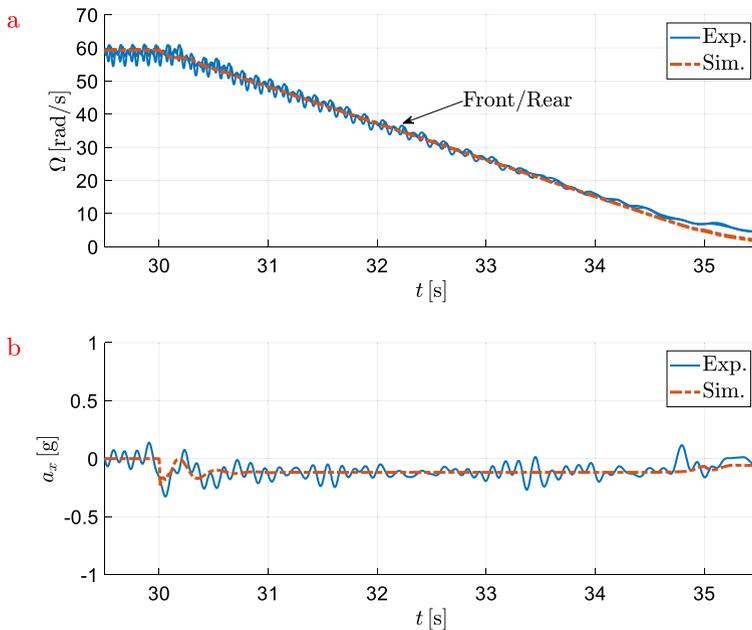
Fig. 18 depicts the errors between the numerical and experimental signals of the human (trunk, thigh, and shank $\omega_{y/z}$) and the vehicle (a_x) considering the maximum (ε_u), the
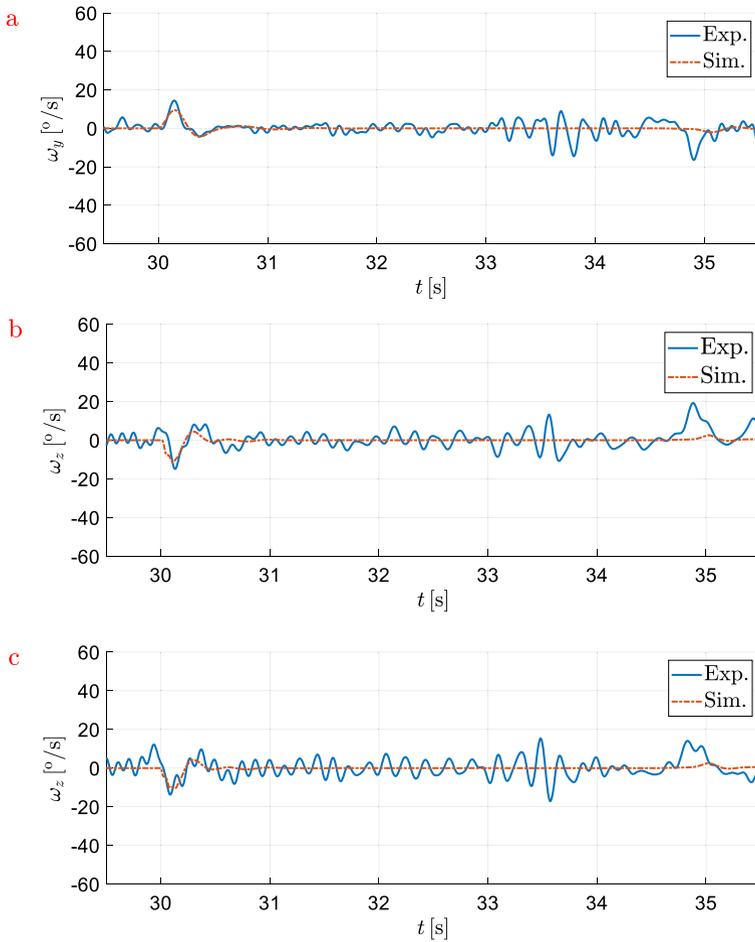
Table 7 Settings of GA

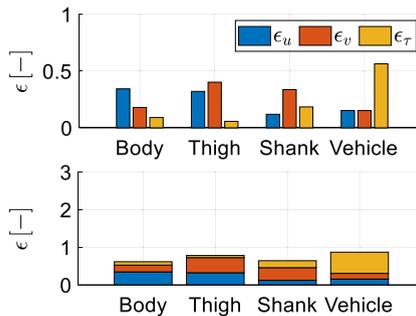| *Population*	
Population size	120
Elite population	5%
Crossover fraction	0.8
Mutation method	gaussian
Stopping criteria	
Maximum number of generations	20
Maximum number of stall generations	3
Cost function tolerance	0.001
Cost function limit	0.5
Time limit	∞

Table 8 Settings of PS

Searching method	
Initial mesh size	0.2
Stopping criteria	
Cost function tolerance	0.001
Step tolerance	0.01
Mesh tolerance	0.001
Maximum number of iterations	20
Time limit	∞

Fig. 16 Experimental and simulated signal comparison: wheel angular velocities (a) and longitudinal acceleration (b) in the light braking maneuver

Fig. 17 Experimental and simulated signal comparison: trunk angular velocities around *y* local axis (a), thigh angular velocity around *z* local axis (b) and shank angular velocity around *z* local axis (c) in the light braking maneuver

Fig. 18 Experimental-numerical error in the light braking maneuver

minimum (ε_v), and their time distance (ε_τ) as shown in Equation (5) in the light braking maneuver.

Data availability No datasets were generated or analysed during the current study.

Declarations

Ethics approval and consent to participate All procedures are conformed to the Helsinki Declaration.

Competing interests The authors declare no competing interests.

References

1. Bozzi, A.D., Aguilera, A.: Shared E-scooters: a review of uses, health and environmental impacts, and policy implications of a new micro-mobility service. Sustainability **13**, 8676 (2021). https://doi.org/10.3390/su13168676
2. Boglietti, S., Barabino, B., Maternini, G.: Survey on e-powered micro personal mobility vehicles: exploring current issues towards future developments. Sustainability **13**, 3692 (2021). https://doi.org/10.3390/su13073692
3. Reck, D.J., Martin, H., Axhausen, K.W.: Mode choice, substitution patterns and environmental impacts of shared and personal micro-mobility. Transp. Res., Part D, Transp. Environ. **102**, 103134 (2022). https://doi.org/10.1016/j.trd.2021.103134
4. Zagorskas, J., Burinskienė, M.: Challenges caused by increased use of e-powered personal mobility vehicles in European cities. Sustainability **12**, 273 (2019). https://doi.org/10.3390/su12010273
5. Almannaa, M.H., Ashqar, H.I., Elhenawy, M., Masoud, M., Rakotonirainy, A., Rakha, H.: A comparative analysis of e-scooter and e-bike usage patterns: findings from the city of Austin, TX. Int. J. Sustain. Transp. **15**, 571–579 (2021). https://doi.org/10.48550/arXiv.2006.04033
6. Leoni, J., Tanelli, M., Strada, S.C., Savaresi, S.M.: Assessing e-scooters safety and drivability: a quantitative analysis. IFAC-PapersOnLine **55**, 260–265 (2022). https://doi.org/10.1016/j.ifacol.2022.10.294
7. Butler, L., Yigitcanlar, T., Paz, A., Areed, W.: How can smart mobility bridge the first/last mile gap? Empirical evidence on public attitudes from Australia. J. Transp. Geogr. **104**, 103452 (2022). https://doi.org/10.1016/j.jtrangeo.2022.103452
8. Paudel, M., Fah Yap, F.: Front steering design guidelines formulation for e-scooters considering the influence of sitting and standing riders on self-stability and safety performance. Proc. Inst. Mech. Eng. Part D, J. Automob. Eng. **235**, 2551–2567 (2021). https://doi.org/10.1177/0954407021992176
9. Maier, O., Györfi, B., Wrede, J., Kasper, R.: Design and validation of a multi-body model of a front suspension bicycle and a passive rider for braking dynamics investigations. Multibody Syst. Dyn. **42**, 19–45 (2018). https://doi.org/10.1007/s11044-017-9576-5
10. Moore, J.K., Kooijman, J.D.G., Schwab, A.L., Hubbard, M.: Rider motion identification during normal bicycling by means of principal component analysis. Multibody Syst. Dyn. **25**, 225–244 (2011). https://doi.org/10.1007/s11044-010-9225-8

11. Jolly, K., Krzywinski, S., Rao, P.V.M., Gupta, D.: Kinematic modeling of a motorcycle rider for design of functional clothing. Int. J. Cloth. Sci. Technol. **31**, 856–873 (2019). https://doi.org/10.1108/IJCST-02-2019-0020
12. Tony, B.J.A.R., Alphin, M.S., Sri Krishnan, G.: Analysis of upper body ergonomic parameters on commuter motorbike users. J. Transp. Health **16**, 100828 (2020). https://doi.org/10.1016/j.jth.2020.100828
13. García-Agúndez Blanco, A., Vallejo, D.G., Freire, E., Agúndez, A.G., García-Vallejo, D., Freire, E., Agúndez, G., García-Vallejo, A., Freire, E.: An electric kickscooter multibody model: equations of motion and linear stability analysis (2023). https://doi.org/10.21203/rs.3.rs-3464019/v1
14. Arslan, E., Uyulan, Ç.: Analysis of an e-scooter and rider system dynamic response to curb traversing through physics-informed machine learning methods. Proc. Inst. Mech. Eng. Part D, J. Automob. Eng. (2022). https://doi.org/10.1177/09544070221100111
15. Asperti, M., Vignati, M., Braghin, F.: Modeling of the vertical dynamics of a kick e-scooter on distributed road irregularity. In: Advances in Dynamics of Vehicles on Roads and Tracks II: Proceedings of the 27th Symposium of the International Association of Vehicle System Dynamics, IAVSD 2021, August 17–19, 2021, Saint Petersburg, Russia, pp. 1070–1080. Springer (2022)
16. Asperti, M., Vignati, M., Braghin, F.: Modelling of the vertical dynamics of an electric kick scooter. IEEE Trans. Intell. Transp. Syst. **23**, 9266–9274 (2021). https://doi.org/10.1109/TITS.2021.3098438
17. Vella, A.D., Vigliani, A.: Research on the longitudinal dynamics of an electric scooter. SAE Int. J. Veh. Dyn. Stab. NVH **7**, 35–51 (2022). https://doi.org/10.4271/10-07-01-0003
18. Cafiso, S., Di Graziano, A., Marchetta, V., Pappalardo, G.: Urban road pavements monitoring and assessment using bike and e-scooter as probe vehicles. Case Stud. Constr. Mater. **16**, 889 (2022). https://doi.org/10.1016/j.cscm.2022.e00889
19. Cano-Moreno, J.D., Cabanellas Becerra, J.M., Arenas Reina, J.M., Islán Marcos, M.E.: Analysis of e-scooter vibrations risks for riding comfort based on real measurements. Machines **10**, 688 (2022). https://doi.org/10.3390/machines10080688
20. Boglietti, S., Ghirardi, A., Zanoni, C.T., Ventura, R., Barabino, B., Maternini, G., Vetturi, D.: First experimental comparison between e-kick scooters and e-bike's vibrational dynamics. Transp. Res. Proc. **62**, 743–751 (2022). https://doi.org/10.1016/j.trpro.2022.02.092
21. Brunner, P., Löcken, A., Denk, F., Kates, R., Huber, W.: Analysis of experimental data on dynamics and behavior of e-scooter riders and applications to the impact of automated driving functions on urban road safety. In: 2020 IEEE Intelligent Vehicles Symposium (IV), pp. 219–225. IEEE (2020)
22. Cano-Moreno, J.D., Islán, M.E., Blaya, F., D'Amato, R., Juanes, J.A., Soriano, E.: E-scooter vibration impact on driver comfort and health. J. Vib. Eng. Technol. 1–15 (2021). https://doi.org/10.1007/s42417-021-00280-3
23. Cano-Moreno, J.D., Marcos, M.I., Haro, F.B., D'Amato, R., Juanes, J.A., Heras, E.S.: Methodology for the study of the influence of e-scooter vibrations on human health and comfort. In: Proceedings of the Seventh International Conference on Technological Ecosystems for Enhancing Multiculturality, pp. 445–451 (2019)
24. Vella, A.D., Digo, E., Gastaldi, L., Pastorelli, S., Vigliani, A.: Statistical analysis of the vibrations transmitted from an electric kick scooter to riders. Exp. Tech. **48**, 803–813 (2024). https://doi.org/10.1007/s40799-023-00693-7
25. Vella, A.D., Digo, E., Gastaldi, L., Pastorelli, S.P., Vigliani, A.: Evaluation of human body kinematics while riding electric kick scooter. In: Mechanisms and Machine Science, pp. 11–17. Springer (2024)
26. Ventura, R., Ghirardi, A., Vetturi, D., Maternini, G., Barabino, B.: A framework for comparing the vibrational behaviour of e-kick scooters and e-bikes. Evidence from Italy. Evidence from Italy. https://doi.org/10.2139/ssrn.4072708
27. Blajer, W., Dziewiecki, K., Mazur, Z.: Multibody modeling of human body for the inverse dynamics analysis of sagittal plane movements. Multibody Syst. Dyn. **18**, 217–232 (2007). https://doi.org/10.1007/s11044-007-9090-2
28. Zanoni, A., Cocco, A., Masarati, P.: Multibody dynamics analysis of the human upper body for rotorcraft–pilot interaction. Nonlinear Dyn. **102**, 1517–1539 (2020). https://doi.org/10.1007/s11071-020-06005-7
29. Ambrósio, J.A.C., Kecskeméthy, A.: Multibody dynamics of biomechanical models for human motion via optimization. In: García Orden, J.C., Goicolea, J.M., Cuadrado, J. (eds.) Multibody Dynamics, pp. 245–272. Springer, Dordrecht (2007)
30. Wang, P., Yi, J., Liu, T.: Stability and control of a rider–bicycle system: analysis and experiments. IEEE Trans. Autom. Sci. Eng. **17**, 348–360 (2019). https://doi.org/10.1109/TASE.2019.2922068
31. Garman, C.M.R., Como, S.G., Campbell, I.C., Wishart, J., O'Brien, K., McLean, S.: Micro-mobility vehicle dynamics and rider kinematics during electric scooter riding. SAE Technical Paper (2020)
32. Digo, E., Pastorelli, S., Gastaldi, L.: A narrative review on wearable inertial sensors for human motion tracking in industrial scenarios. Robotics **11** (2022). https://doi.org/10.3390/robotics11060138

33. Vella, A.D., Digo, E., Vigliani, A.: Experimental analysis and multibody simulation of electric kick scooter braking maneuver. In: IFToMM World Congress on Mechanism and Machine Science, pp. 533–540. Springer, Berlin (2024)
34. MathWorks: Simscape^{TM} Multibody^{TM} Reference. Natick (2023)
35. Besselink, I.J.M., Schmeitz, A.J.C., Pacejka, H.B.: An improved Magic Formula/Swift tyre model that can handle inflation pressure changes. Veh. Syst. Dyn. **48**, 337–352 (2010). https://doi.org/10.1080/00423111003748088
36. Shampine, L.F., Reichelt, M.W., Kierzenka, J.A.: Solving index-1 DAEs in Matlab and Simulink. SIAM Rev. **41**, 538–552 (1999). https://doi.org/10.1137/S003614459933425X
37. Poulet, Y., Brassart, F., Simonetti, E., Pillet, H., Faupin, A., Sauret, C.: Analyzing intra-cycle velocity profile and trunk inclination during wheelchair racing propulsion. Sensors **23** (2023). https://doi.org/10.3390/s23010058
38. Regterschot, G.R.H., Zhang, W., Baldus, H., Stevens, M., Zijlstra, W.: Accuracy and concurrent validity of a sensor-based analysis of sit-to-stand movements in older adults. Gait Posture **45**, 198–203 (2016). https://doi.org/10.1016/j.gaitpost.2016.02.004
39. Pacejka, H.: Tire and Vehicle Dynamics. Elsevier, Amsterdam (2005)
40. Conn, A.R., Gould, N.I.M., Toint, P.: A globally convergent augmented Lagrangian algorithm for optimization with general constraints and simple bounds. SIAM J. Numer. Anal. **28**, 545–572 (1991)
41. Conn, A., Gould, N., Toint, P.: A globally convergent Lagrangian barrier algorithm for optimization with general inequality constraints and simple bounds. Math. Comput. **66**, 261–288 (1997)
42. Audet, C., Dennis, J.E. Jr: Analysis of generalized pattern searches. SIAM J. Optim. **13**, 889–903 (2002)
43. Kolda, T.G., Lewis, R.M., Torczon, V.: Optimization by direct search: new perspectives on some classical and modern methods. SIAM Rev. **45**, 385–482 (2003)